Macromolecules

ARTICLE

pubs.acs.org/Macromolecules

Morphology and Conductivity in Ionic Liquid Incorporated Sulfonated Block Copolymers

Sung Yeon Kim,[†] Eunjin Yoon,[‡] Taiha Joo,[‡] and Moon Jeong Park*[,†,‡]

[†]Division of Advanced Materials Science (WCU) and [‡]Department of Chemistry, Pohang University of Science and Technology (POSTECH), Pohang, Korea 790-784

ABSTRACT: We have explored the link between morphologies and conductivities for ionic liquids (ILs) incorporated block copolymer electrolytes by combining small-angle X-ray scattering, transmission electron microscopy, and impedance spectroscopy. The block copolymer electrolytes investigated in present study are a series of partially sulfonated poly(styrenesulfonate-*b*-methylbutylene) (S_nMB_m) copolymers with different molecular weights and sulfonation levels (SLs). Imidazolium-based ILs are selectively doped into hydrophilic domains of S_nMB_m copolymers, and various morphologies have been observed as a function of the amount of absorbed ILs and SLs in S_nMB_m copolymers. We have demonstrated that the morphologies of ILs impregnated S_nMB_m copolymers are sensitive function of kinds of counteranions in IL, yielding remarkable discrepancy in conductivities. When the morphology of sample is appeared to be a lamellar structure, significant reduction in through-plane conductivity value was detected due to the nonrandom orientation of microdomains. In contrast, hexagonally perforated lamellar forming samples exhibit the highest conductivities in both through-plane and in-plane directions on account of the better connectivity of ionic domains along the perforated hydrophilic phases. Once the morphology effects were vanished by employing highly sulfonated S_nMB_m copolymers, it has been revealed that the conductivities of ILs incorporated copolymers are closely related to the polarity of ILs as confirmed by solvation dynamics study.

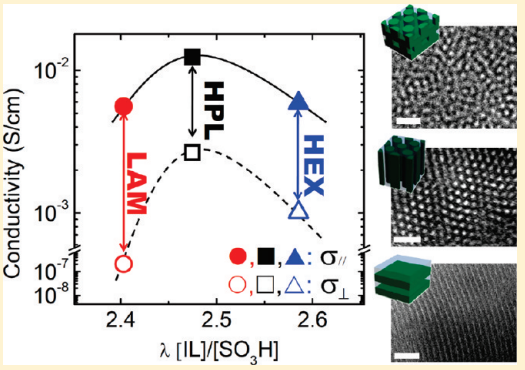

INTRODUCTION

Proton exchange fuel cell (PEFC) has been extensively investigated in past decades due to their potential to supply clean energy for transport applications.[1−7] In early years, the researches on PEFC had focused on room temperature operation,[1,2] and many issues such as CO poisoning of Pt catalyst and the complexity of water management in polymer electrolyte membranes (PEMs) have been revealed.[8−10] Several approaches are in progress to overcome these problems, and operating PEFC at high temperature above 120 °C under nonhumidification conditions is considered to be the most promising solution.[11−22] This is due to the fact that CO poisoning becomes negligible above 120 °C and transport kinetics are significantly enhanced at high temperatures.[23,24]

For the high temperature PEFC, there is a growing need to find new PEM systems offering reasonable proton conductivity without water. For example, although the current state-of-the-art PEM, perfluorosulfonic acid ionomer commercialized under the trademark Nafion, shows excellent conductivity and long-term durability at low temperature,[1,2] the properties rapidly decay at elevated temperatures since water is lost from the PEM.[25−27] Most widely studied approach to develop new PEM systems in recent years is the fabrication of composite PEMs by incorporating ionic liquids (ILs) to replace water molecule. ILs are molten salts exhibiting nonvolatility, thermal stability, negligible vapor pressures, and excellent ionic conductivity at high temperature, which will alleviate the durability concerns.[28−34] Examples of the composite PEMs are perfluorosulfonic acid membranes (Nafion),[11−16] sulfonated poly(aryl ether ketone) (SPAEK),[13−15] and sulfonated poly(ether ether ketone) (SPEEK),[18] impregnated with a variety of ILs. The reported conductivity values are as high as 10^{-3}−10^{-2} S/cm at 180 °C when large amounts of ILs are incorporated.[13−18] However, the conductivity is unsatisfactory when compared to the properties obtained at humidified conditions, and further improvements are required.

To achieve improved conductivities of IL incorporated PEMs, the fundamental underpinning of morphology-transport relationship in composite PEMs and systematic methodology to control morphologies of PEMs are essential. However, all above systems, i.e., Nafion, SPAEK, and SPEEK, have disordered morphologies due to the random location of the hydrophilic and hydrophobic moieties resulting in a lack of knowledge on the morphology−conductivity relationship in composite PEMs. With this regard, most recently, a great attention has been paid to PEMs made from block copolymers[22,33−43] due to their self-assembly nature, originated from the balance of energetic and entropic driving forces.[44,45] Examples include sulfonated poly(styrene-*b*-methyl methacrylate),[22] sulfonated poly(styrene-*b*-methylbutylene),[35] poly(styrene-*b*-vinylpyridine),[36−38] and poly(vinylidene fluoride-*co*-hexafluoropropylene).[39,40] It has

Received: February 7, 2011
Revised: June 2, 2011
Published: June 15, 2011

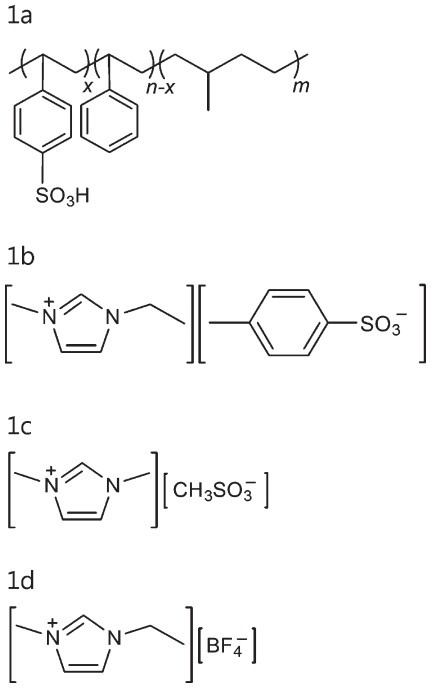

Figure 1. Molecular structures of (a) poly(styrenesulfonate-*b*-methylbutylene) (S_nMB_m) copolymer, (b) 1-ethyl-3-methylimidazolium tosylate, [EMIm][Tos], (c) 1,3-dimethylimidazolium methanesulfonate, [MMIm][MS], and (d) 1-ethyl-3-methylimidazolium tetrafluoroborate, [EMIm][BF4].

been reported that altering processing conditions such as solvent casting and thermal annealing conditions induce great different morphologies in PEMs and concurrently result in diverse windows of conductivity in PEMs.[22,46] In a recent paper,[35] we demonstrated that the development of composite PEMs with well-defined nanostructures plays a central role to achieve enhanced conductivity by creating shortcut of ion transport.

Many previous studies on IL incorporated PEMs are concerned with the morphological transitions of composite PEMs by changing the IL concentrations and their effects on conductivities.[36−38,41−43] In those cases, the analysis of morphology effects on conductivities is not straightforward because of the concurrent contributions arising from morphology and local IL concentration. The different morphologies are also accessible by altering molecular weight of PEMs enough to hop the phase boundaries; however, molecular weight effects on ion transport will coincide with the morphology effects. Herein, we have explored the morphology effects on conductivities of IL incorporated PEMs using a set of partially sulfonated poly(styrene-*b*-methylbutylene), which referred to S_nMB_m copolymers. The S_nMB_m copolymers, exploited by our group recently,[35,46−49] will be the ideal materials to overcome the above-mentioned limitations on account of their unique self-assembly nature. At fixed IL concentrations, small changes in sulfonation levels (SLs) of sulfonated styrene (SS) phases of S_nMB_m copolymers (without changing n and m values) result in a wide variety of morphologies such as lamellar (LAM), hexagonally perforated lamellae (HPL), and hexagonal cylinder (HEX) phases. This phase behavior leads us to determine the morphology effects on conductivities of composite PEMs with excluded influence of IL concentrations and molecular weight of PEMs. Note that the SL in PEMs is also known to be an important parameter affecting conductivity, and thus, the SL effects cannot be downplayed. However, in the present study, we found that the normalization of conductivities based on SLs was found to be an effective way to eliminate the SL effects. By employing various imidazolium-based ILs, we have demonstrated that the different kinds of anions in ILs induce distinctly different morphologies of composite PEMs, leading to remarkable discrepancy in conductivities at the same IL loadings.

EXPERIMENTAL SECTION

Synthesis of S_nMB_m Copolymers. A series of S_nMB_m copolymers with different molecular weights and SLs were synthesized by sequential anionic polymerization of styrene and isoprene followed by selective hydrogenation of the polydiene. The polydispersity indices of the copolymers were less than 1.04. The styrene blocks were then sulfonated using procedures described in refs 35 and 49. Samples with different SLs were prepared by controlling reaction time: SL = 17 ± 3 mol % with 0.25 h reaction, SL = 37 ± 4 mol % with 1 h reaction, SL = 49 ± 2 mol % with 4 h reaction, and SL = 63 ± 3 mol % with 25 h reaction. The molecular structure of resulting materials is shown in Figure 1a where SL of S_nMB_m was calculated by the following equation:

$$\mathrm{SL} = \frac{\text{moles of sulfonic acid}}{\text{moles of styrene}} = \frac{x}{n} \quad (1)$$

The SL value of the copolymer is given in parentheses; i.e., $S_{50}MB_{73}(21)$ contains 50 styrene chains and 73 methylbutylene chains where 21 mol % of styrene is sulfonated. The characteristics of S_nMB_m copolymers used in this study are listed in Table 1.

Ionic Liquids (ILs). 1-Ethyl-3-methylimidazolium tosylate ([EMIm][Tos], ≥98% HPLC grade), 1,3-dimethylimidazolium methanesulfonate ([MMIm][MS], ≥99% HPLC grade), and 1-ethyl-3-methylimidazolium tetrafluoroborate ([EMIm][BF4], ≥98% HPLC grade) were purchased from Sigma-Aldrich and used as received. The molecular structures of [EMIm][Tos], [MMIm][MS], and [EMIm][BF4] are shown in parts b, c, and d of Figure 1, respectively. The [Tos] and [MS] anions were chosen so as to contain sulfonate groups to ensure chemical similarity with SS phases. The molecular weight (MW), density (d), melting temperature (T_m), and conductivity (σ) are listed in Table 1.

Preparation of IL Incorporated S_nMB_m Membranes. Inhibitor-free anhydrous tetrahydrofuran (THF, ≥99.9%) was used without further purification, and methanol was degassed three times prior to use. In the glovebox, predetermined quantities of IL and S_nMB_m were weighed into glass vials, and ca. 5 wt % solutions were prepared using 50/50 vol % THF and methanol mixture. Solutions were stirred overnight at room temperature, and ca. 200 μm thick IL incorporated S_nMB_m membranes were prepared by solvent casting under an argon atmosphere for 2 days followed by vacuum drying at 50 °C for 10 days.

Small-Angle X-ray Scattering (SAXS). The composite membranes were laminated into an airtight sample cell consists of an aluminum spacer, two Kapton windows, O-rings, and aluminum covers. The samples were stored with desiccant when outside the glovebox to reduce any chance of water contamination. Synchrotron SAXS measurements on these samples were performed using the 4C1 SAXS beamline at the Pohang Light Source (PLS). Sample temperature was controlled within ±0.2 °C using a sample stage provided by the PLS. The wavelength (λ) of the incident X-ray beam was 0.15 nm ($\Delta\lambda/\lambda = 10^{-4}$), and two sample-to-detector distances of 3.0 and 1.0 m were used yielding scattering wave vector q ($q = 4\pi \sin(\theta/2)/\lambda$, where θ is the scattering angle) in the range 0.1−1.8 nm^{-1}. The resulting two-dimensional scattering data were averaged azimuthally to obtain intensity versus q.

Transmission Electron Microscopy (TEM). The composite membranes were cryo-microtomed at −120 °C to obtain thin sections

Table 1. Characteristics of S_nMB_m Block Copolymers and Ionic Liquids Used in the Present Study

block copolymer used	MW (kg/mol)	SL (mol %)	IEC (mmol/g)	ionic liquids used	MW (g/mol)	d (g/cm^3)	T_m (°C)	$\sigma_\perp$ (mS/cm)
$S_{50}MB_{73}(21)$	5.9-*b*-5.1	21	0.901	[MMIm][MS][a]	192.24		98.3[e]	45.9[e] (135 °C)
$S_{50}MB_{73}(39)$	6.7-*b*-5.1	39	1.673	[EMIm][BF4][b]	197.97	1.28[d]	11−15[d]	41.0[e] (135 °C)
$S_{50}MB_{73}(66)$	7.8-*b*-5.1	66	2.55	[EMIm][Tos][c]	282.36	1.21[f]	58[e]	17.0[e] (135 °C)
$S_{89}MB_{130}(19)$	10.3-*b*-9.1	19	0.862					
$S_{89}MB_{130}(39)$	11.8-*b*-9.1	39	1.616					
$S_{89}MB_{130}(49)$	12.6-*b*-9.1	49	2.011					

[a] 1,3-Dimethylimidazolium methanesulfonate. [b] 1-Ethyl-3-methylimidazolium tetrafluoroborate. [c] 1-Ethyl-3-methylimidazolium tosylate. [d] Reference 14. [e] Measured at our lab. [f] Reference 61.

with thicknesses in the 80−120 nm range using a Leica Ultracut UCT. The electron contrast in the samples was enhanced by exposure to ruthenium tetroxide (RuO_4) vapor for 50 min. Imaging of stained samples was performed with a JEOL JEM-2100F microscope operating at 200 kV equipped with a cold stage (−160 °C) and an Omega energy filter. Images were recorded on a Gatan 2048 × 2048 pixel CCD camera (Gatan Inc., Pleasanton, CA). All data sets were acquired using Digital Micrograph (Gatan, Inc.) software.

Conductivity Measurements. The conductivities of IL incorporated S_nMB_m samples were measured using ac impedance spectroscopy in glovebox. The in-plane conductivity was measured using a four-electrode probe (BekkTech LLC, Loveland, CO), consisting of a Teflon block, a membrane clamp, two platinum gauzes, and two platinum wires. The two platinum wires were used as working and counter electrodes to apply a current to the sample membrane (2.0 cm × 1.0 cm, 200 μm thick) through the two platinum gauzes, and the two platinum wires 0.425 cm apart were used as reference electrodes. The through-plane conductivity was measured using a home-built two-electrode cell with 1.25 cm × 1.25 cm two stainless steel blocking electrodes and 1 cm × 1 cm Pt working/counter electrodes. For conductivity measurements, the highest temperature of our experimental setup was 180 °C (simply due to the thermal stability of the sheath of cables). We then calibrated the sample temperature accurately, which yields the highest sample temperature of 165 and 145 °C for 4-probe and 2-probe geometry, respectively. Data were collected using a 1260 Solatron impedance analyzer operating over a frequency range of 1−100000 Hz.

Solvation Dynamics Measurements. Time-resolved fluorescence spectra were recorded by the time-correlated single photon counting (TCSPC) method. Details of the TCSPC setup has been described elsewhere.[50] Light source was a femtosecond Ti:sapphire oscillator (Tsunami, Spectra Physics) that gives pulses at 800 nm with a pulse duration of 100 fs. Pump pulses at 400 nm were generated by the second harmonic generation in a β-barium borate crystal. Fluorescence was collected by a parabolic mirror, dispersed by a monochromator, and detected with a fast photomultiplier tube. Magic angle detection was used to avoid the effect of polarization. Full width at half-maximum of the instrumental response was 190 ps to provide ∼40 ps time resolution after deconvolution. Time traces in the range of 470−700 nm were obtained by a 10 nm step size and reconstructed to give the time-resolved fluorescence spectra. Laser grade coumarin 153 (C153) from Exciton was used without further purification. C153 was dissolved in two different ILs, [EMIm][Tos] and [MMIm][MS], and the measurements were performed at 98 °C, which is above the melting temperature of the ILs.

RESULTS

Characteristics of S_nMB_m Copolymers and Ionic Liquids. Figure 1a shows the chemical structure of S_nMB_m copolymer, where n and m indicate degree of polymerization of each blocks. The characteristics of S_nMB_m copolymers used in present study are listed in Table 1. The SL values of S_nMB_m copolymers are given in parentheses. The S_nMB_m copolymers have been known to offer substantial proton conductivity under low-temperature conditions, and the conductivity can be easily adjustable by controlling molecular weight and ion exchange capacity (IEC) of copolymers.[46,47] Note here that the IEC values of S_nMB_m copolymers range from 0.86 to 2.55 mmol/g, which are fairly wide windows compared to other PEM systems.

Parts b, c, and d of Figure 1 show chemical structures of ILs used in present study, 1-ethyl-3-methylimidazolium tosylate ([EMIm][Tos]), 1,3-dimethylimidazolium methanesulfonate ([MMIm][MS]), and 1-ethyl-3-methylimidazolium tetrafluoroborate ([EMIm][BF4]), respectively. All ILs contain alkylimidazolium cations while kinds of anions are varied. The molecular weight (MW), density (d), melting temperature (T_m), and conductivity (σ) are listed in Table 1. It should be noted here that since the [Tos] and [MS] anions show chemically identical or similar structures to the SS moiety of S_nMB_m copolymers, the good compatibility between copolymers and ILs is expected. In contrast, the [BF4] anion represents dissimilar chemical structure with the SS moiety although [EMIm][BF4] is one of the most widely used IL with perfluorinated membranes such as Nafion.[11−16] We are aimed to investigate the compatibility effects on morphologies and conductivities of IL loaded S_nMB_m copolymers. Note that all ILs, i.e., [EMIm][Tos], [MMIm][MS], and [EMIm][BF4], indicate hydrophilic characteristics.

Morphology of Ionic Liquid Incorporated S_nMB_m Copolymers. We begin by describing the morphologies of IL incorporated S_nMB_m copolymers as a function of the amount of absorbed IL by combining SAXS and TEM experiments. For brevity, we only discuss representative data obtained from a subset of the samples listed in Table 1. The entire samples examined in this study indicate temperature-independent SAXS profiles. Figure 2 shows the SAXS profiles of [EMIm][Tos] incorporated $S_{50}MB_{73}(21)$ membranes with different IL loadings measured at 120 °C. The neat $S_{50}MB_{73}(21)$ exhibits LAM morphology with Bragg peaks (↓) at q^*, $2q^*$, and $3q^*$, where $q^* = 2\pi/d_{100}$ with d_{100} = 10.9 nm. Qualitatively different SAXS peaks are observed with 30 wt % IL loading in $S_{50}MB_{73}(21)$, as shown by inverted filled triangles (▼), where the presence of Bragg peaks at $1q^*$:$\sqrt{3}q^*$:-$\sqrt{4}q^*$:$\sqrt{9}q^*$ with $q^* = 2\pi/d_{100}$ and d_{100} = 13.4 nm is seen. The SAXS profile indicates the formation of a hexagonally ordered structure. TEM was used to determine the observed morphology as HPL or HEX phases. The inset TEM image of Figure 2 presents the coexistence of short lamellae with perforations and a hexagonal arrangement of the perforations (SS phases are darken by RuO_4 staining), which leads us to conclude that the structure is HPL. When the amount of IL is increased to 50 wt %, we see broad peaks at $1q^*$:$2q^*$:$3q^*$ with $q^* = 0.41$ nm^{-1}. This implies that the morphology becomes ill-defined at high IL loadings, as

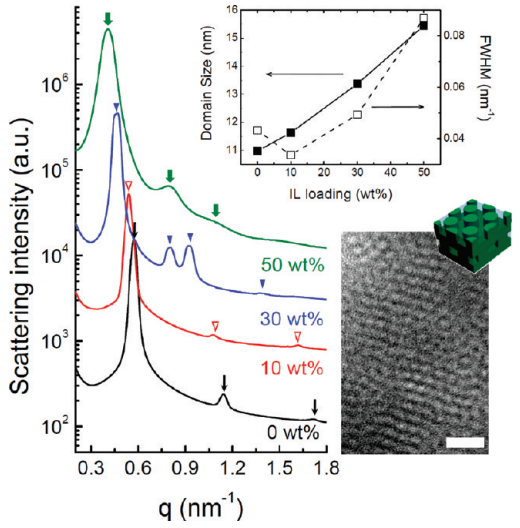

Figure 2. SAXS profiles of [EMIm][Tos] incorporated $S_{50}MB_{73}(21)$ measured at 120 °C as a function of IL loadings. The scattering profiles are vertically offset for clarity. The arrows (black ↓) for 0 wt % IL, the inverted open triangles (▽) of 10 wt % IL, the inverted filled triangles (▼) of 30 wt % IL, and the inverted thick arrows (green ↓) indicate Bragg peaks at q^*, $2q^*$, $3q^*$; at q^*, $2q^*$, $3q^*$; at q^*,$\sqrt{3}q^*$,$\sqrt{4}q^*$,$\sqrt{9}q^*$; and at q^*, $2q^*$, $3q^*$; respectively. The changes in domain spacing and fwhm of primary peak as a function of IL loadings are plotted in the inset figure. Cross-sectional TEM image obtained with 30 wt % IL loading confirms the HPL phase. SS domains were darkened by RuO_4 staining, and the scale bars represent 50 nm.

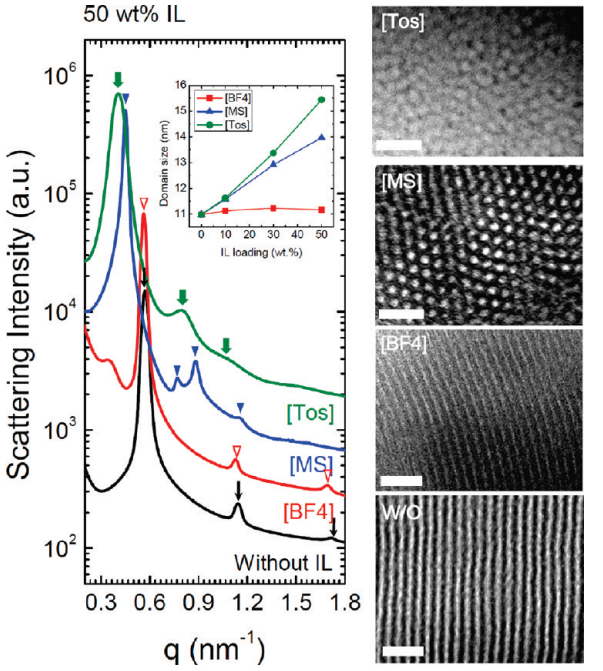

Figure 3. SAXS profiles and TEM images of IL incorporated $S_{50}MB_{73}$-(21) copolymers by varying kinds of ILs at a fixed IL loading of 50 wt %. The scattering profiles are vertically offset for clarity. The arrows (black ↓, neat), the inverted open triangles (▽, [BF4]), the inverted filled triangles (▼, [MS]), and the inverted thick arrows (green ↓, [Tos]) indicate Bragg peaks at q^*, $2q^*$, $3q^*$; at q^*, $2q^*$, $3q^*$; at q^*,$\sqrt{3}q^*$,$\sqrt{4}q^*$,$\sqrt{7}q^*$; and at q^*, $2q^*$, $3q^*$; respectively. The changes in domain spacing are plotted in the inset figure as a function of IL loadings. TEM images of no IL, [EMIm][BF4], [MMIm][MS], and [EMIm]-[Tos] incorporated $S_{50}MB_{73}(21)$ copolymers represent LAM, LAM, HEX, and spherical domains, respectively. The SS domain was darkened by RuO_4 staining, and the scale bars represent 50 nm.

viewed by large increase in the full width at half-maximum (fwhm) of the primary peak at 50 wt % IL loading (see the inset of Figure 2).

It is worthwhile to mention here that, upon undergoing the morphological transitions given in Figure 2, significant increases in domain sizes are observed in proportion to the [EMIm][Tos] concentrations, as shown in the inset of Figure 2. This implies that the incorporation of [EMIm][Tos] results in effective swelling of hydrophilic SS phases presumably due to the chemical similarity of [Tos] anions with the SS moieties. The observed sequential lyotropic phase transitions can be mapped on to the phase diagram of block copolymer/solvent systems. In pioneering studies, Lodge et al. showed that the phase behavior of block copolymer/selective solvent mixtures can be understood in terms of effective χ parameters.[51] The extent to which such a framework can be applied to our systems although, direct comparisons between nonionic block copolymers and our ionic S_nMB_m copolymers may not be appropriate because of the presence of ionic interactions in our systems. We carried out the order−disorder transition (ODT) study for low molecular weight $S_{24}MB_{37}(19)$ sample, and it is found that the LAM morphology becomes disordered at 75 °C (neat $S_{24}MB_{37}(19)$) and 120 °C (30 wt % [EMIm][Tos] incorporated $S_{24}MB_{37}(19)$) (data not shown here). Consequently, we can infer that phase transitions of [EMIm][Tos] containing S_nMB_m copolymers are taken place with increasing volume fraction of hydrophilic PSS block as well as the enhanced segregation strength between hydrophilic and hydrophobic phases.[44,45] The quantitative analysis of the effective χ parameters of composite membranes will be subject of our future paper.

To investigate the effect of kinds of anions in ILs on the morphological transitions of S_nMB_m copolymers, the same experimental protocols are repeated with other ILs, i.e., [MMIm][MS] and [EMIm][BF4]. Figure 3 shows the representative SAXS data and cross-sectional TEM images obtained from different IL incorporated $S_{50}MB_{73}(21)$ copolymers at a fixed IL loading of 50 wt %. The distinctly different morphologies depending on the choice of anions in ILs are seen. For example, when 50 wt % of [EMIm][BF4] is added into $S_{50}MB_{73}(21)$ copolymer, qualitatively the same LAM structure has been detected with the q^*:$2q^*$:$3q^*$ Bragg peaks (▽). In addition, as shown in the inset of Figure 3, a fairly small change in domain size was observed. This clearly indicates poor miscibility of fluorinated [BF4] anion with hydrocarbon SS phases, which is proven by the existence of an additional peak at lower q value (q = 0.37 nm^{-1}), signaling the existence of ionic aggregates in the membrane. The LAM morphology of 50 wt % [EMIm][BF4] doped $S_{50}MB_{73}(21)$ copolymer was confirmed by TEM as shown in Figure 3. It is interesting to mention here that although the SAXS data indicate similar LAM structure for neat $S_{50}MB_{73}$-(21) and 50 wt % [EMIm][BF4] doped $S_{50}MB_{73}(21)$, the TEM image reveals relatively thick SS phases of 50 wt % [EMIm][BF4] doped $S_{50}MB_{73}(21)$ compared with the neat sample. The domain spacing of [EMIm][BF4] incorporated sample, obtained from both SAXS and TEM, is the same as ca. 11 nm. This indicates that although the negligible change in domain size is detected, the ionic SS phases is somewhat swollen by the [EMIm][BF4] due to the hydrophilic characteristics. We assume

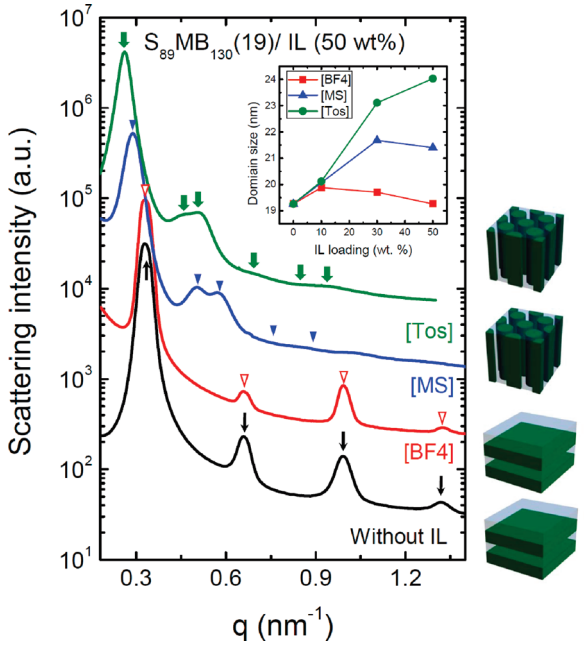

Figure 4. SAXS profiles of IL incorporated $S_{89}MB_{130}(19)$ copolymers by varying kinds of ILs at the same IL loading of 50 wt %. The scattering profiles are vertically offset for clarity. The arrows (black ↓) (neat copolymer) and the inverted open triangles (▽) (with [EMIm][BF4]) indicate Bragg peaks at q^*, $2q^*$, $3q^*$, $4q^*$ while the inverted filled triangles (▼) (with [MMIm][MS]) and the inverted thick arrows (green ↓) (with [EMIm][Tos]) represent Bragg peaks at q^*,$\sqrt{3}q^*$,$\sqrt{4}q^*$,$\sqrt{7}q^*$,$\sqrt{9}q^*$, $\sqrt{11}q^*$. The changes in domain spacing as a function of IL loadings are plotted in the inset figure. The schematic illustration of each nanostructure is shown in the right-hand side of each SAXS profile representing LAM, LAM, HEX, and HEX morphologies.

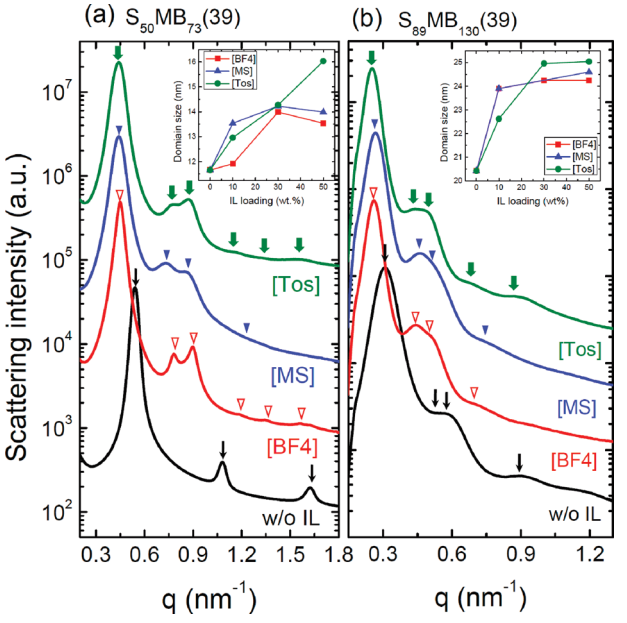

Figure 5. SAXS profiles of 30 wt % IL incorporated (a) $S_{50}MB_{73}(39)$ and (b) $S_{89}MB_{130}(39)$ copolymers by varying kinds of ILs. The arrows (↓) of neat $S_{50}MB_{73}(39)$ with Bragg peaks at q^*, $2q^*$, $3q^*$ and of neat $S_{89}MB_{130}(39)$ with peaks at q^*,$\sqrt{3}q^*$,$\sqrt{4}q^*$,$\sqrt{9}q^*$ indicate LAM and HEX morphologies, respectively. Upon adding 30 wt % of IL, regardless of kinds of ILs, all SAXS profiles show Bragg peaks at q^*,$\sqrt{3}q^*$,$\sqrt{4}q^*$,$\sqrt{7}q^*$,$\sqrt{9}q^*$,$\sqrt{11}q^*$ indicative of the HEX morphology. The changes in domain size as a function of IL loadings are plotted in the inset. The scattering profiles are vertically offset for clarity.

that some extent of [EMIm][BF4] also exists in PMB domains at higher IL loadings, but the exact nature of hydrophobic PMB domains cannot be determined from our work thus far. The detailed distribution of [EMIm][BF4] within the microdomains of S_nMB_m copolymers will be a subject of our future studies.

Upon incorporating 50 wt % of [MMIm][MS] into the same $S_{50}MB_{73}(21)$ copolymer, HEX structure is appeared, as confirmed by both SAXS and TEM. The increments in domain size is relatively smaller than that obtained with [EMIm][Tos]. We infer that degree of swelling with [MS] anions is to some extent modest compared with [Tos] anions, in part, due to the smaller anion size. When the increments in domain size are compared for 10 wt % IL containing $S_{50}MB_{73}(21)$ copolymers where all samples indicate LAM morphology, the values are 1.3%, 5.4%, and 5.8% for [EMIm][BF4], [MMIm][MS], and [EMIm]-[Tos], respectively. The ill-defined morphology of 50 wt % [EMIm][Tos] doped $S_{50}MB_{73}(21)$ is identified as spherical domains lacking long-ranged order, as shown in the inset TEM image.

We found that the observed IL-dependent morphologies of composite membranes are not sensitive function of molecular weight of S_nMB_m copolymers. When large molecular weight $S_{89}MB_{130}(19)$ with similar n/m ratio and SL is employed, the qualitatively similar SAXS profiles to those shown in Figure 3 have been observed. Figure 4 shows SAXS profiles of different ILs incorporated $S_{89}MB_{130}(19)$ copolymers at a fixed IL concentration of 50 wt %. The neat $S_{89}MB_{130}(19)$ copolymer indicates LAM morphology with Bragg peaks (↓) at q^*, $2q^*$, $3q^*$, and $4q^*$, where $q^* = 2\pi/d_{100}$ with d_{100} = 19.3 nm. Analogous to $S_{50}MB_{73}$-(21) copolymer, the incorporation of 50 wt % [EMIm][BF4] reveals LAM morphology with negligible change in domain size while the addition of 50 wt % [MMIm][MS] induces LAM-to-HEX morphological transition. The addition of 50 wt % [EMim][Tos] also results in HEX morphology. For HEX forming samples with 50 wt % ILs, the changes in domain sizes are 13% and 26% for [MMIm][MS] and [EMIm][Tos], respectively. It seems that the degree of swelling of the large molecular weight $S_{89}MB_{130}(19)$ in the presence of ILs is clearly smaller than that of lower molecular weight $S_{50}MB_{73}(21)$ presumably due to the rather stiff characteristics of $S_{89}MB_{130}(19)$. In general, however, the phase behavior is qualitative comparable and the sequence of swelling (inferred from changes in domain size) is [BF4] < [MS] < [Tos]. From the data obtained so far, we have reached to the conclusion that the chemical structures of anions strongly affect the morphologies of composite membranes.

To investigate the effect of ionic strength of S_nMB_m copolymers on the observed phase behavior, the SLs of copolymers have been varied. Figure 5 shows the SAXS profiles of 30 wt % IL incorporated $S_{50}MB_{73}(39)$ and $S_{89}MB_{130}(39)$ copolymers. Since these copolymers contain almost twice number of [$-SO_3H$] groups, i.e., more hydrophilic nature of SS phases, favorable uptake of ILs within ionic domains is expected. As seen from Figure 5a,b, the neat $S_{50}MB_{73}(39)$ and $S_{89}MB_{130}(39)$ copolymers show LAM and HEX structures with Bragg peaks at q^*:$2q^*$:$3q^*$ and q^*:$\sqrt{3}q^*$:$\sqrt{4}q^*$:$\sqrt{9}q^*$, respectively. When the different ILs are loaded into the copolymers at a fixed concentration of 30 wt %, interestingly, virtually no difference in morphologies has been detected. For example, as shown in Figure 5a, the

dx.doi.org/10.1021/ma200278c |Macromolecules 2011, 44, 5289–5298

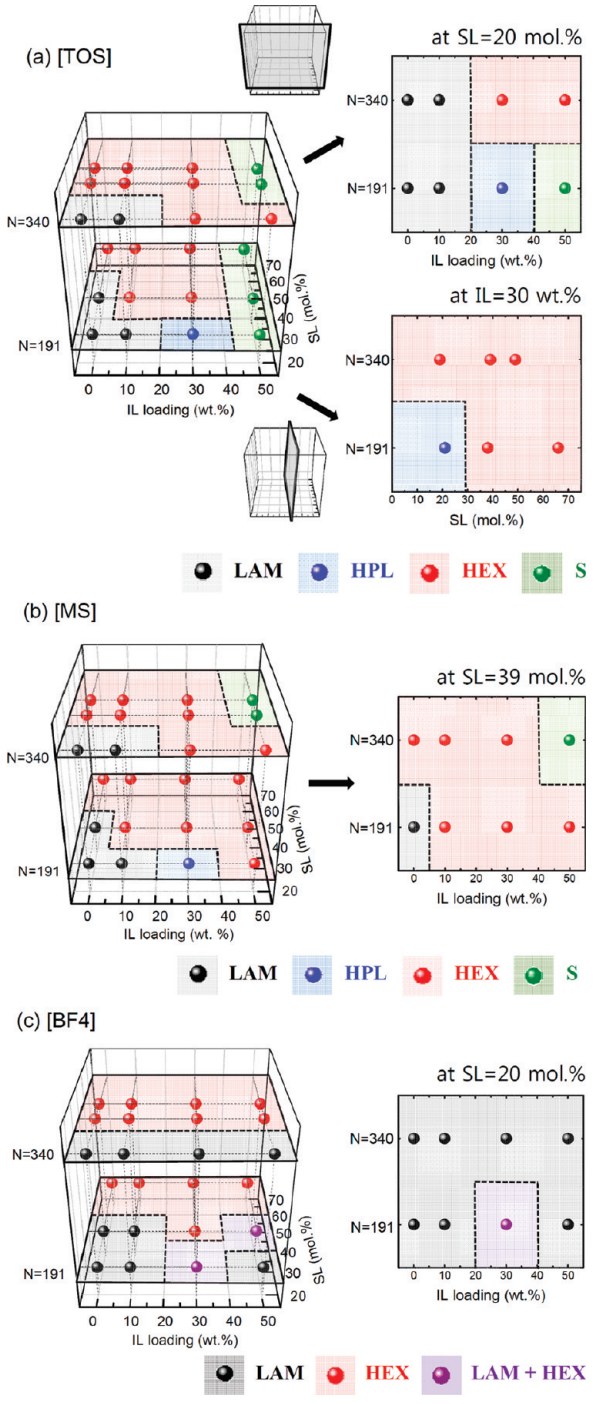

Figure 6. (a) 3-Dimensional phase cube of [EMIm][Tos] incorporated S_nMB_m copolymers as a function of IL loading, sulfonation level (SL), and degree of polymerization (N), of S_nMB_m:$S_{50}MB_{73}$ series (N = 191) and $\mathbf{S_{50}MB_{73}}$ series (N = 340). The phase boundaries are marked with dotted lines. 2D phase diagrams of N vs IL loading (front view) and N vs SL (side view) at a given SL of 20 mol % and IL of 30 wt % are plotted on the right-hand side of the phase cube, which represents cross sections of the cube. LAM, HPL, HEX, and S indicate lamellae, hexagonally perforated lamellae, hexagonal cylinder, and spherical domains, respectively. 3D phase cubes of (b) [MMIm][MS] and (c) [EMIm][BF4] incorporated S_nMB_m copolymers as a function of IL loading, SL, and N of S_nMB_m. 2D phase diagrams of N vs IL loading plots (front view) obtained at given SL values are shown in the right-hand side of each phase cube.

same HEX phases are seen from Bragg peaks at q^*:$\sqrt{3}q^*$:-$\sqrt{4}q^*$:$\sqrt{7}q^*$:$\sqrt{9}q^*$:$\sqrt{11}q^*$ for 30 wt % IL loaded $S_{50}MB_{73}(39)$ copolymers regardless of kinds of ILs. This is sharp contrast to what observed with $S_{50}MB_{73}(21)$. However, as shown in the inset of Figure 5a, the extent of swelling of $S_{50}MB_{73}(39)$ copolymer with different ILs still follows the same trend as [BF4] < [MS] < [Tos].

Figure 5b shows the phase behavior of ILs doped $S_{89}MB_{130}$-(39) copolymers, which is analogous to Figure 5a where the same HEX morphologies are seen regardless of kinds of ILs. From inset plots in Figure 5a,b, the increments in domain sizes of the $S_nMB_m(39)$ copolymers upon incorporating [EMIm][BF4] become considerably larger than those of the S_nMB_m copolymers with SL = 20 ± 1 mol %. This behavior can be rationalized by the increased compatibility between [BF4] anions and PSS phase upon adding more [$-SO_3H$] groups into SS phases. Consequently, there is no doubt about the role of ionic strength of the S_nMB_m copolymers on determining the ability of IL uptake, which eventually results in different phase behavior of IL-doped membranes.

Phase Diagrams of Ionic Liquid Incorporated S_nMB_m Copolymers. On the basis of the methodology described above, the phase diagrams of IL incorporated S_nMB_m copolymers as a function of the amounts of ILs loading, degree of polymerization (N), and SL of copolymers are plotted inside a cube in Figure 6. N is calculated based on $N = (\nu_S/\nu_0)N_S + (\nu_{MB}/\nu_0)N_{MB}$ with a reference volume, ν_0, of 0.1 nm^3, S segment volume, ν_S, of 0.167 nm^3, and MB segment volume, ν_{MB}, of 0.147 nm^3, neglecting the small change in N upon sulfonation. The letters LAM, HPL, HEX, and S indicate lamellae, hexagonally perforated lamellae, hexagonal cylinder, and spherical domains, respectively, and the dotted lines show the phase boundaries. The left and back side of the cube at 0 wt % IL indicates the phase behavior of neat S_nMB_m copolymers plotted as N vs SL. The neat S_nMB_m copolymers show the LAM morphology at lower SL values while large windows of phase diagram are occupied by HEX phase at higher SL values. In all cases, there are no accessible order−disorder transition temperatures up to 180 °C, and thus the T-axis is omitted for clarity.

In Figure 6a, the phase cube of [EMIm][Tos] incorporated S_nMB_m copolymers is shown. A variety of morphologies such as LAM, HPL, HEX, and S are seen. A large portion of the phase cube is taken up by the HEX phase for both N = 191 and N = 340 samples while HPL phase was only visible with N = 191 sample. This implies that the stability window of the HPL morphology becomes narrower and eventually disappears with increase in molecular weight. We also plot 2-dimensional (2D) phase diagrams on the right-hand side of the 3D phase cube in Figure 6a representing cross sections of the cube. Upon creating a cross section along SL = 20 mol %, for example, a phase diagram of N vs IL loading (front view) illuminates the [EMIm][Tos] amount dependent morphologies of $S_nMB_m(20)$ copolymers. Another 2D phase diagram of N vs SL (side view) intersects the N vs IL loading plots, indicating SL-dependent phase behavior of S_nMB_m copolymers, at a fixed amount of IL. A typical example obtained at 30 wt % IL loading is shown.

Phase behavior of [MMIm][MS] incorporated S_nMB_m copolymers and [EMIm][BF4] doped copolymers is also depicted in parts b and c of Figure 6, respectively. It is evident that the phase behavior of [MMIm][MS]-doped S_nMB_m copolymers is qualitatively similar to that obtained with [EMIm][Tos] owing to the possession of sulfonate groups. The N vs IL loading plots

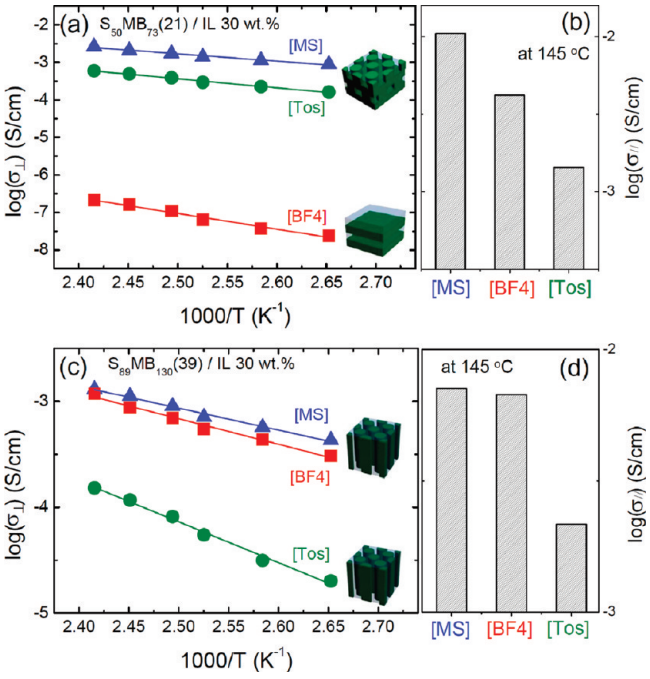

Figure 7. (a, c) Temperature-dependent through-plane conductivities ($\sigma_\perp$) and (b, d) in-plane conductivities ($\sigma_\parallel$) of IL incorporated $S_{50}MB_{73}$ (21) and $S_{89}MB_{130}$ (39) copolymers, as indicated in the figure. The conductivity values were obtained at a fixed IL concentration of 30 wt %, and the types of IL are indicated in the figure. In (a) and (c), the linear fits were obtained by Arrhenius plots. The schematic illustration of each nanostructure is also shown. In (b) and (d) the representative $\sigma_\parallel$ values obtained at 145 °C are shown.

obtained at a given SL of 39 mol % is shown on right-hand side of the cube as a representative example where a large portion of HEX phase is seen at high SL values.

In contrast, with the addition of [EMIm][BF4], distinctly different phase behavior is observed as shown in Figure 6c. For S_nMB_m copolymers possessing low SL values, the LAM phase persists at high IL loadings, regardless of N. This is due to the poor compatibility between fluorinated [BF4] anions with SS ionic moieties. As shown in Figure 6c, 2D phase diagram obtained with SL = 20 mol % indicates coexistence between LAM and HEX phases over a substantial portion of the accessible IL loading−SL window for N = 191 samples while such coexistence is not detected with N = 340 samples. At higher SL values, HEX phase is mostly seen in the phase cube, and we were unable to detect the spherical domains owing to the relatively small swelling of SS phases in the presence of [BF4] anions. Note that all observed morphologies for [EMIm][BF4] containing S_nMB_m copolymers are thermally stable with multiple heating/cooling cycles from 25 to 180 °C. The phase diagrams in Figure 6a−c clearly suggest to us the uniqueness of our systems in the aspect of designing desired morphologies of IL incorporated PEMs by independent controls of the kinds of ILs, N, and SL of copolymers. It should be noted here that due to the coarse steps in the amounts of IL, other phases may exist at intermediate IL loadings.

DISCUSSION

Morphology Effects of IL Incorporated S_nMB_m Copolymers on Ionic Conductivities. We now elucidate the morphology effects on ion transport properties for the IL incorporated S_nMB_m copolymers. Ionic conductivities of composite membranes were measured using ac impedance spectroscopy over a frequency range of 1−100000 Hz by employing a 1260 Solartron impedance analyzer. To exclude the issue of water contamination of hygroscopic samples, sample preparations and measurements were performed under Ar-filled glovebox with moisture concentration below 0.1 ppm. Conductivity measurements through plane of the membrane ($\sigma_\perp$) were determined with the use of a two-electrode cell while in-plane conductivities ($\sigma_\parallel$) were measured using a four-electrode cell probe (BekkTech conductivity clamp). The $\sigma_\perp$ values were always lower than the $\sigma_\parallel$ values in consequence of the coincidence of the current path and voltage sensing cable. In particular, the lack of equality of $\sigma_\parallel$ and $\sigma_\perp$ is occasionally observed for many block copolymer based PEMs due to the nonrandom domain orientation in the samples.[22,35,46,52−54] In present study, typically observed anisotropy in conductivities of IL doped S_nMB_m copolymers is $\sigma_\parallel/\sigma_\perp$ = 4−7.

Two sets of conductivity data are shown in Figure 7. The $\sigma_\perp$ and $\sigma_\parallel$ values shown in parts a and b of Figure 7, respectively, are obtained from 30 wt % IL loaded $S_{50}MB_{73}$(21) by varying kinds of ILs. As seen in Figure 7a, the $\sigma_\perp$ values of the membranes lie in order of [MS] > [Tos] ≫ [BF4]: $\sigma_\perp$ = 2.65 [MS], $\sigma_\perp$ = 0.596 [Tos], and $\sigma_\perp = 2.08 \times 10^{-4}$ mS/cm [BF4] at 141 °C. This is in sharp contrast to the sequence of $\sigma_\parallel$ values, as plotted in Figure 7b, where the magnitude of $\sigma_\parallel$ values is [MS] > [BF4] > [Tos]: $\sigma_\parallel$ = 10.49 [MS], $\sigma_\parallel$ = 4.21 [BF4], and $\sigma_\parallel$ = 1.43 mS/cm [Tos] at 145 °C. Note that the highest temperature accessible with the four-electrode cell probe was 165 °C, and the data will be discussed in Figure 9.

Without a doubt the large reduction in $\sigma_\perp$ of the [EMIm][BF4]-doped sample is on account of the morphology effect. In ref 35, we demonstrated that the parallel orientation of LAM morphology is naturally developed during solvent casting process for the $S_{50}MB_{73}$(21)/[EMIM][BF4] sample. Such anisotropy in morphology significantly hinders ion conduction in the through-plane direction due to the alternating sequence of conducting/nonconducting domains. As a result, a large anisotropy in conductivity occurs with $\sigma_\parallel/\sigma_\perp$ ratio of 2.0×10^4. Qualitatively similar behavior is observed for all other LAM forming samples.

When highly sulfonated samples are employed to exclude the morphology effects, judged by the large occupation of HEX phase in phase diagrams, remarkably, both $\sigma_\perp$ and $\sigma_\parallel$ provide us the same order of [MS] ≳ [BF4] > [Tos]. As shown in Figure 7c, d, when 30 wt % IL is loaded in $S_{89}MB_{130}$(39) copolymer, the obtained conductivity values are $\sigma_\parallel$ = 7.1 and $\sigma_\perp$ = 1.3 mS/cm ([MMIm][MS], $\sigma_\parallel/\sigma_\perp$ = 5.5), $\sigma_\parallel$ = 6.7 and $\sigma_\perp$ = 1.2 mS/cm ([EMIM][BF4], $\sigma_\parallel/\sigma_\perp$ = 5.6), and $\sigma_\parallel$ = 2.2 and $\sigma_\perp$ = 0.15 mS/cm ([EMIM][Tos], $\sigma_\parallel/\sigma_\perp$ = 14.7). The relatively large reduction in the $\sigma_\perp$ value with [EMIm][Tos] is not clearly understood yet. From the slope of Arrhenius plots, the activation energy (E_a) of composite membranes are estimated at 23.2 ± 2.6, 27.9 ± 5.2, and 44.6 ± 11.1 kJ/mol for 30 wt % [MMIm][MS], [EMIm][BF4], and [EMIm][Tos] loadings, respectively. It is interesting to note here that for [MMIm][MS] incorporated samples the E_a values are nonsensitive function of SL or molecular weight of S_nMB_m copolymers. Instead, the E_a values are highly susceptible of the amounts of IL within the membranes. For instance, the E_a value of 50 wt % [MMIm][MS] containing $S_{50}MB_{73}$(21) is significantly low as 13.8 kJ/mol.

The coincident trend in $\sigma_\parallel$ and $\sigma_\perp$ of the composite membranes with vanished morphology effect (Figure 7c,d) leads us to

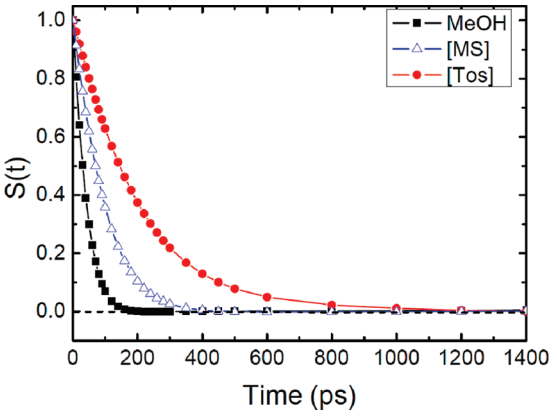

Figure 8. Time-dependent Stokes shift functions for coumarin 153 (C153) in methanol (■), [MMIm][MS] (△), and [EMIm][Tos] (●).

study the reason why the conductivities of IL incorporated S_nMB_m copolymers lie in order of [MS] ≳ [BF4] > [Tos]. In particular, an explanation about low conductivity values obtained with [EMIm][Tos] loadings, which is one-third of the values of [MMIm][MS] incorporated samples, is aimed to be provided. As mentioned in Figures 3 and 4, the [Tos] has been proven to be the best compatible anions with our S_nMB_m copolymers.

The origin of the IL-dependent conductivities was investigated by examining the solvation dynamics of ILs. Solvation dynamics is a key ingredient in modeling how charge transfer reactions couple to a solvent environment.[55,56] In particular, fluctuation of the solvent coordinate is thought to be rate limiting for certain barrierless charge-transfer reactions.[57] One of the most popular methods of estimating the solvation dynamics is to acquire the dynamic Stokes shift function $S(t)$ from the time-resolved fluorescence spectra of a probe molecule in solution:

$$S(t) = \frac{\overline{\omega}(t) - \overline{\omega}(\infty)}{\overline{\omega}(0) - \overline{\omega}(\infty)} \qquad (2)$$

where $\bar{\omega}(t)$ denotes the average frequency of the fluorescence spectrum at time t. We measured time-resolved fluorescence spectra of coumarin 153 (C153) in the ILs to estimate the solvation dynamics. The fluorescence band of C153, carrying intramolecular charge transfer character, is known to be a sensitive probe of the solvent polarization.[58,59] Average frequencies of the fluorescence spectra of C153 at times t were obtained to calculate $S(t)$.

Figure 8 shows $S(t)$ of C153 in [EMIm][Tos] and [MMIm][MS]. The $S(t)$ of C153 in methanol is also shown as a reference. The $S(t)$ were fitted to an exponential function to give the time constants of 96, 200, and 40 ps for [MMIm][MS], [EMIm][Tos], and methanol, respectively. The solvation time of methanol was overestimated due to the limited time resolution; it is known to be 10 ps.[58] The smaller time constant in [MMIm][MS] indicates relatively faster solvation than that in [EMIm][Tos]. This could be intimately related to the enhanced ion transport rate in [MMIm][MS] incorporated S_nMB_m copolymers, since the faster solvent fluctuation may stimulate the faster cation−anion dissociation dynamics in the presence of imidazolium solvating [$-SO_3H$] groups. The solvation time constant for [EMIm][BF4] was reported to be 125 ps.[60] This is in good agreement with our conductivity data, where similar but larger conductivity values are always obtained with the use of [MMIm][MS] compared with the use of [EMIm][BF4] when the morphology effect is vanished.

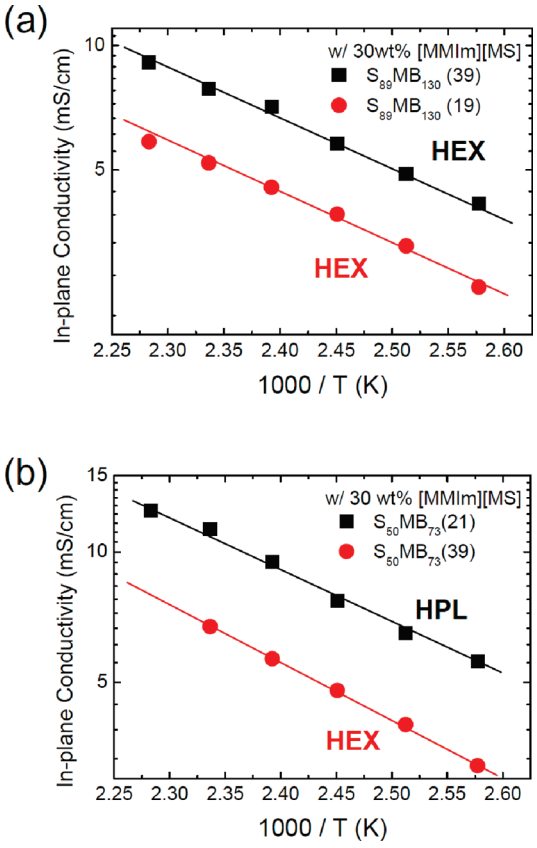

Figure 9. Temperature-dependent in-plane conductivities of 30 wt % [MMIm][MS] incorporated S_nMB_m copolymers obtained under anhydrous conditions: (a) with vanished morphology effects and (b) in the presence of morphology effects.

We hope to conclude our paper by summarizing all factors, which make effects on the conductivity. First of all, the SL in PEMs is known to be one of the important parameter affecting conductivity. In present study, we found that as far as morphology is unchanged, the conductivity value is more like proportional to the SL ratio of copolymers if the same amounts of IL are incorporated. Figure 9a,b shows the in-plane conductivity values of 30 wt % [MMIm][MS] incorporated $S_{89}MB_{130}$ and $S_{50}MB_{73}$ samples by varying the SLs. As shown in Figure 9a, for $S_{89}MB_{130}$ copolymers with SL = 19% and SL = 39%, both samples indicate HEX morphology at 30 wt % [MMIm][MS] loading, and the observed conductivity ratio is 1.7 ± 0.2 for temperature window from 115 to 165 °C. This ratio is in good agreement with the SL ratio of 2.0. In contrast, when the samples show different morphologies, the normalization was no more effective. As seen from Figure 9b, HPL forming $S_{50}MB_{73}(21)$ with 30 wt % [MMIm][MS] loading indicates higher conductivity than that of HEX forming $S_{50}MB_{73}(39)$ with 30 wt % [MMIm][MS]. This is presumably due to the better connectivity of ionic domains along the perforated SS phases. It is worthwhile to emphasize that the sample with lower SL yields higher conductivity, which leads us to conclude that the relative impact of SLs on the conductivity is not as radical as the morphology effects.

The morphology effects on the conductivity were examined in more details by plotting the data obtained from various kinds of

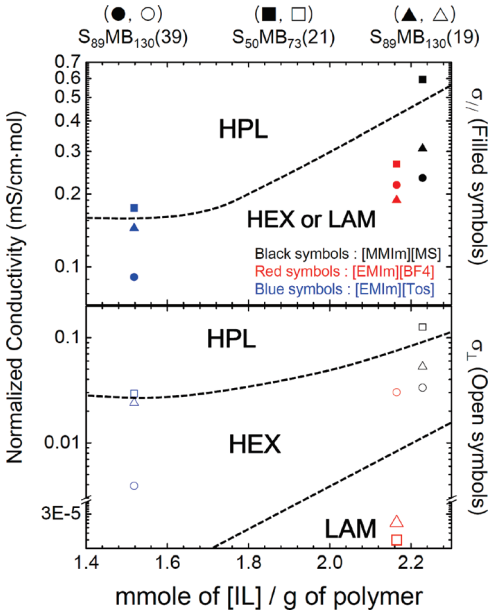

Figure 10. In-plane ($\sigma_{\parallel}$, filled symbols) and through-plane conductivities ($\sigma_{\perp}$, open symbols) of 30 wt % IL incorporated S_nMB_m copolymers obtained at 165 °C under anhydrous conditions. The IL loading in weight fraction is converted to the mmole of absorbed [IL]/g of polymer. Three different S_nMB_m copolymers (plotted with different symbols) and three different ILs (shown with different color) are used as indicated in the figure.

ILs. The amount of absorbed IL was recalculated on the basis of mmoles of IL per grams of polymers, λ, which can accurately reflect the different molecular weight of ILs used in present study. The conductivity values obtained at 165 °C under anhydrous conditions are normalized based on the SL. We plot the normalized in-plane ($\sigma_{\parallel}$, filled symbols) and through-plane ($\sigma_{\perp}$, open symbols) conductivities of IL incorporated S_nMB_m copolymers in Figure 10 as a function of λ. Although the x-axis of Figure 10 represents different λ values depending on kinds of ILs, they all correspond to the same IL loading of 30 wt %. The normalized conductivity data obtained from three different copolymers are shown with different symbols, as indicated in the figure. The black, red, and blue colored symbols represent the conductivity values of [MMIm][MS], [EMIm][BF4], and [EMIm][Tos] loaded S_nMB_m copolymers, respectively.

As seen in the figure, the [MMIm][MS] doped samples always yield the highest conductivity regardless of molecular weight and SL of S_nMB_m copolymers. When the morphology effect is vanished by increasing SL in S_nMB_m copolymers, the [EMIm]-[BF4] incorporated samples indicate quite similar conductivity as the [MMIm][MS] loaded samples in both in-plane (●) and through-plane (○) directions. In fact, for the S_nMB_m copolymers with higher SL, due to the large E_a values with [EMIm][BF4] (e.g., Figure 7c), the conductivity of [EMIm][BF4] incorporated samples may overtake that of [MMIm][MS] containing ones at very high temperature. This is presumably due to the increased compatibility between [BF4] anions and PSS phase upon adding more [$-SO_3H$] groups into SS phases, as we discussed in Figure 5. On the contrary, clearly low conductivity values were obtained with [EMIm][Tos] loadings.

When the morphology of sample is appeared to be LAM with the use of [EMIm][BF4] and S_nMB_m copolymers possessing low SL, significant reduction in $\sigma_{\perp}$ values was detected as indicated with larger open symbols. This is because through-plane conductivity requires connectivity of microdomains along the thickness direction and obtaining this in parallel oriented LAM is not feasible. The higher conductivity for the HPL-forming sample than other morphologies is also observed with the use of [EMIm][Tos] in both directions, although the difference in conductivity between HPL and HEX was not so distinct compared with the result obtained with [MMIm][MS]. The ability to control the conductivity of IL doped PEMs by adjusting kinds of ILs and the morphologies of composite membranes will allow us not only to resolve links between morphology and transport in quantitative way but also to achieve efficient ion transport in PEMs for high-temperature fuel cell applications.

CONCLUSIONS

We have investigated phase behavior and conductivity of IL incorporated S_nMB_m block copolymers by controlling the kinds of ILs, N, and SLs of S_nMB_m copolymers. Various morphologies such as lamellae, perforated lamellae, hexagonal cylinder, and spherical domains have been observed depending on SLs of S_nMB_m copolymers and/or the amount of absorbed ILs. S_nMB_m copolymers possessing lower SL values indicate lower IL uptake ability, and the observed morphologies of IL incorporated S_nMB_m copolymers are sensitive function of kinds of ILs. For example, the addition of [EMIm][BF4] results in small changes in morphology compared with neat copolymers. In contrast, in the presence of [EMIm][Tos] and [MMIm][MS], the copolymers indicate effective swelling of hydrophilic domains and concomitant morphological transitions with increase in the amounts of IL loading. The different morphologies yield significant discrepancy in conductivity values at the same IL concentration. It has been shown that the [MMIm][MS] incorporated samples exhibiting hexagonally perforated lamellar structure show utmost conductivity while [EMIm][BF4] loaded lamellar forming samples indicate large reduction in through-plane conductivity. When S_nMB_m copolymers with higher SL are employed, the effect of kinds of ILs on the morphology becomes negligible due to the enhanced ability of IL uptake. With vanished morphology effect, conductivities of samples largely depend on the polarity of ILs.

AUTHOR INFORMATION

Corresponding Author

*E-mail: moonpark@postech.edu.

ACKNOWLEDGMENT

This work was financially supported by Basic Science Research Program through the National Research Foundation of Korea (NRF) funded by the Ministry of Education, Science and Technology (Project No. 2011-0004375) and WCU (World Class University) program through the Korea Science and Engineering Foundation funded by the Ministry of Education, Science and Technology (Project No. R31-10059). SAXS measurements were conducted on the beamline 4C1 at the Pohang Light Source (PLS) supported by the Ministry of Science and Technology of Korea. TEM was performed at the National Nanofab Center supported by Korea Nano Technology Research Society (Project No. N100810002).

REFERENCES

(1) Hickner, M. A.; Ghassemi, H.; Kim, Y. S.; Einsla, B. R.; McGrath, J. E. *Chem. Rev.* **2004**, *104*, 4587–4611.
(2) Mauritz, K. A.; Moore, R. B. *Chem. Rev.* **2004**, *104*, 4535–4585.
(3) Devanathan, R. *Energy Environ. Sci.* **2008**, *1*, 101–119.
(4) Higashihara, T.; Matsumoto, K.; Ueda, M. *Polymer* **2009**, *50*, 5341–5357.
(5) Wang, Y.; Chen, K. S.; Mishler, J.; Cho, S. C.; Adroher, X. C. *Appl. Energy* **2011**, *88*, 981–1007.
(6) Elabd, Y. A.; Hickner, M. A. *Macromolecules* **2011**, *44*, 1–11.
(7) Peckham, T. J.; Holdcroft, S. *Adv. Mater.* **2010**, *22*, 4667–4690.
(8) Li, Q.; He, R.; Gao, J. A.; Jensen, J. O.; Bjerrum, N. J. *J. Electrochem. Soc.* **2003**, *150* (12), A1599–A1605.
(9) Li, Q.; He, R.; Jensen, J. O.; Bjerrum, N. J. *Chem. Mater.* **2003**, *15*, 4896–4915.
(10) Schuster, M. F. H.; Meyer, M. H. *Annu. Rev. Mater. Res.* **2003**, *33*, 233–261.
(11) Sun, W.; Li, X.; Jiao, K. *Electroanalysis* **2009**, *21* (8), 959–964.
(12) Bennett, M. D.; Leo, D. J.; Wilkes, G. L.; Beyer, F. L.; Pechar, T. W. *Polymer* **2006**, *47*, 6782–6796.
(13) Cho, E. K.; Park, J. S.; Sekhon, S. S.; Park, G. G.; Yang, T. H.; Lee, W. Y.; Kim, C. S.; Park, S. B. *J. Electrochem. Soc.* **2009**, *156* (2), B197–B202.
(14) Sekhon, S. S.; Park, J. S.; Baek, J. S.; Yim, S. D.; Yang, T. H.; Kim, C. S. *Chem. Mater.* **2010**, *22* (3), 803–812.
(15) Sekhon, S. S.; Park, J. S.; Cho, E. K.; Yoon, Y. G.; Kim, C. S.; Lee, W. Y. *Macromolecules* **2009**, *42* (6), 2054–2062.
(16) Mistry, M. K.; Subianto, S.; Choudhury, N. R.; Dutta, N. K. *Langmuir* **2009**, *25* (16), 9240–9251.
(17) Deligöz, H.; Yılmazoğlu, M. *J. Power Sources* **2011**.
(18) Che, Q.; Sun, B.; He, R. *Electrochim. Acta* **2008**, *53*, 4428–4434.
(19) Yan, F.; Yu, S.; Zhang, X.; Qiu, L.; Chu, F.; You, J.; Lu, J. *Chem. Mater.* **2009**, *21* (8), 1480–1484.
(20) Nakajima, H.; Ohno, H. *Polymer* **2005**, *46*, 11499–11504.
(21) Missan, H. P. S.; Lalia, B. S.; Karan, K.; Maxwell, A. *Mater. Sci. Eng., B* **2010**, *175*, 143–149.
(22) Gwee, L.; Choi, J. H.; Winey, K. I.; Elabd, Y. A. *Polymer* **2010**, *51*, 5516–5524.
(23) Zhang, J.; Xie, Z.; Zhang, J.; Tang, Y.; Song, C.; Navessin, T.; Shi, Z.; Song, D.; Wang, H.; Wilkinson, D. P.; Liu, Z. S.; Holdcroft, S. *J. Power Sources* **2006**, *160*, 872–891.
(24) Kim, S. K.; Kim, T. H.; Jung, J. W.; Lee, J. C. *Polymer* **2009**, *50*, 3495–3502.
(25) Kreuer, K. D.; Paddison, S. J.; Spohr, E.; Schuster, M. *Chem. Rev.* **2004**, *104*, 4637–4678.
(26) Jiang, R.; Kunz, H. R.; Fenton, J. M. *J. Power Sources* **2005**, *150*, 120–128.
(27) Gebel, G. *Polymer* **2000**, *41*, 5829–5838.
(28) Ueki, T.; Watanabe, M. *Macromolecules* **2008**, *41* (11), 3739–3749.
(29) Xue, H.; Verma, R.; Shreeve, J. M. *J. Fluorine Chem.* **2006**, *127*, 159–176.
(30) Armand, M.; Endres, F.; MacFarlane, D. R.; Ohno, H.; Scrosati, B. *Nature Mater.* **2009**, *8*, 621–629.
(31) Fuller, J.; Breda, A. C.; Carlin, R. T. *J. Electrochem. Soc.* **1997**, *144*, L67–L70.
(32) Susan, M. A. B. H.; Kaneko, T.; Noda, A.; Watanabe, M. *J. Am. Chem. Soc.* **2005**, *127*, 4976–4983.
(33) Chen, H.; Choi, J. H.; Cruz, D. S. D. L.; Winey, K. I.; Elabd, Y. A. *Macromolecules* **2009**, *42*, 4809–4816.
(34) Brown, R. H.; Duncan, A. J.; Choi, J. H.; Park, J. K.; Wu, T.; Leo, D. J.; Winey, K. I.; Moore, R. B.; Long, T. E. *Macromolecules* **2010**, *43*, 790–796.
(35) Kim, S. Y.; Kim, S. H.; Park, M. J. *Nat. Commun.* **2010**, *1*: 88.
(36) Virgili, J. M.; Hexemer, A.; Pople, J. A.; Balsara, N. P.; Segalman, R. A. *Macromolecules* **2009**, *42*, 4604–4613.
(37) Virgili, J. M.; Nedoma, A. J.; Segalman, R. A.; Balsara, N. P. *Macromolecules* **2010**, *43*, 3750–3756.
(38) Virgili, J. M.; Hoarfrost, M. L.; Segalman, R. A. *Macromolecules* **2010**, *43*, 5417–5423.
(39) Lalia, B. S.; Yamada, K.; Hundal, M. S.; Park, J. J.; Park, G. G.; Lee, W. Y.; Kim, C. S.; Sekhon, S. S. *Appl. Phys. A: Mater. Sci. Process.* **2009**, *96*, 661–670.
(40) Fernicola, A.; Panero, S.; Scrosati, B. *J. Power Sources* **2008**, *178*, 591–595.
(41) Simone, P. M.; Lodge, T. P. *ACS Appl. Mater. Interfaces* **2009**, *1*, 2812–2820.
(42) Simone, P. M.; Lodge, T. P. *Macromolecules* **2008**, *41*, 1753–1759.
(43) Wanakule, N. S.; Virgili, J. M.; Teran, A. A.; Wang, Z. G.; Balsara, N. P. *Macromolecules* **2010**, *43*, 8282–8289.
(44) Leibler, L. *Macromolecules* **1980**, *13*, 1602–1617.
(45) Khandpur, A. K.; Förster, S.; Bates, F. S.; Hamley, I. W.; Ryan, A. J.; Bras, W.; Almdal, K.; Mortensen, K. *Macromolecules* **1995**, *28*, 8796–8806.
(46) Park, M. J.; Balsara, N. P. *Macromolecules* **2010**, *43* (1), 292–298.
(47) Park, M. J.; Downing, K. H.; Jackson, A.; Gomez, E. D.; Minor, A. M.; Cookson, D.; Weber, A. Z.; Balsara, N. P. *Nano Lett.* **2007**, *7* (11), 3547–3552.
(48) Kim, S. Y.; Park, M. J. *Macromolecules* **2010**, *43*, 8128–8135.
(49) Park, M. J.; Balsara, N. P. *Macromolecules* **2008**, *41* (10), 3678–3687.
(50) Manoj, P.; Min, C.-K.; Aravindakumar, C. T.; Joo, T. *Chem. Phys.* **2008**, *352*, 333–338.
(51) Hanley, K. J.; Lodge, T. P.; Huang, C.-I. *Macromolecules* **2000**, *33*, 5918.
(52) Elabd, Y. A.; Walker, C. W.; Beyer, F. L. *J. Membr. Sci.* **2004**, *231*, 181–188.
(53) Chen, H.; Palmese, G. R.; Elabd, Y. A. *Chem. Mater.* **2006**, *18*, 4875–4881.
(54) Maki-Ontto, R.; de Moel, K.; Polushkin, E.; van Ekenstein, G. A.; ten Brinke, G.; Ikkala, O. *Adv. Mater.* **2002**, *14*, 357–361.
(55) Sumi, H.; Marcus, R. A. *J. Chem. Phys.* **1986**, *84*, 4272.
(56) Sumi, H.; Marcus, R. A. *J. Chem. Phys.* **1986**, *84*, 4894.
(57) Kang, T. J.; Jarzeba, W.; Barbara, P. F.; Fonseca, T. *Chem. Phys.* **1990**, *149*, 81.
(58) Horng, M. L.; Gardecki, J. A.; Papazyan, A.; Maroncelli, M. *J. Phys. Chem.* **1995**, *99*, 17311.
(59) Eom, I.; Joo, T. *J. Chem. Phys.* **2009**, *131*, 244507.
(60) Mandal, P. K.; Saha, S.; Karmakar, R.; Samanta, A. *Curr. Sci.* **2006**, *90* (3), 301–310.
(61) Hernǎndez-Fernǎndez, F. J.; Rĭos, A. P.; Gómez, D.; Rubio, M.; Tomǎs-Alonso, F.; Víllora, G. *Fluid Phase Equilib.* **2008**, *263*, 190–198.